

A hemispherical–directional reflectance model as a tool for understanding image distinctions between cultivated and uncultivated bare surfaces

Jerzy Cierniewski^{a,*}, Tomasz Gdala^b, Arnon Karnieli^c

^a*Institute of Physical Geography and Environmental Planning, Adam Mickiewicz University, Fredry 10, 61-701 Poznan, Poland*

^b*Mathematics and Computer Science Faculty, Adam Mickiewicz University, Poland*

^c*The Remote Sensing Laboratory, Jacob Blaustein Institute for Desert Research, Ben Gurion University of the Negev, Israel*

Received 1 September 2003; received in revised form 6 January 2004; accepted 14 January 2004

Abstract

This paper discusses a model to predict the normalized hemispherical–directional reflectance function for soil or rocky surfaces of a given roughness under conditions of outdoor illumination. These surfaces are simulated by geometrical shapes similar to beads merging into each other, characterized by three parameters. In addition, the shape of the surface is characterized by the directivity factor D_R , expressing the differences between the maximum and the minimum deviations of its height, calculated along all possible directions. The surface is illuminated by a hemispherical light source created by a number of point sources of given light intensities. The light energy is scattered from the surface, in accordance with the quasi-Lambertian function. The distribution of the surface reflectance, as viewed from all the possible directions, can be described for all the possible illumination conditions expressed by the solar zenith and the horizontal angles for a given hemisphere light distribution of a definite optical thickness. This represents the hemispherical–directional reflectance distribution function, HDRDF, of the surface. The HDRDF function is normalized to the nadir viewpoint and visualized for a given illumination condition. The model assumes that the HDRDF of a surface contains information about the directivity of the surface shape, as described by the directivity factor of the surface hemispherical–directional reflectance function D_{HDRDF} . This factor, expressing the asymmetry of the HDRDF with respect to the solar principal plane (SPP), is strongly correlated with the D_R . The use of both factors, the D_R and D_{HDRDF} , enables us to understand the distinctions between soil surface images with height irregularities of directional character that create a furrow microrelief, and irregularities spread non-directly, randomly, depending on whether the soil has been cultivated or not. The model was tested on directional reflectance data measured in the visible, the near and the middle infrared spectra for cultivated surface with furrows, as well as for three uncultivated desert loess and rocky surfaces situated in Israel.

© 2004 Elsevier Inc. All rights reserved.

Keywords: Soil; Bidirectional reflectance; Hemispherical–directional reflectance; Geometrical model

1. Introduction

Natural surfaces in the optical domain show variation in their radiance due to the direction of irradiating solar and sky energy and the direction along which the reflected energy is viewed. Most soils and vegetation canopies are characterized by a clear reflectance peak, called the “hot spot”, viewed along the direction of the backscattering. This phenomenon is explained by a coherent backscatter, if the surfaces contain abundant scatterers that are of the order of the relevant wavelength, or by shadow-hiding, if the scatterers are large as compared with the wavelength of the

incident light and cast well-defined shadow areas on the surfaces. Results of experiments carried out by [Hapke et al. \(1996\)](#) imply that only certain surfaces, such as mosses with small cell structures or dry fine clay-sized particles, might have a hot spot caused by coherent backscatter. However, shadow-hiding typifies the hot spot behavior of most vegetation canopies, including broad-leaved and coniferous ones, as well as the majority of soil surfaces. Opaque rough soil surfaces with irregularities caused by the soil texture, aggregates and microrelief configurations that are large compared to the wavelength of the incident light, produce shadow areas in which the solar beams do not directly reach the surface even under clear sky conditions. Wave energy leaving these shadow areas is many orders-of-magnitude smaller than energy reflected from sunlit soil fragments. Thus, cultivated soils with dominant diffuse features usually

* Corresponding author. Tel.: +48-61-8294583; fax: +48-618295480.
E-mail address: ciernje@amu.edu.pl (J. Cierniewski).

seem to be the brightest from the direction that gives the lowest proportion of shaded fragments. This is the backscattering direction towards the sun's position for which each scatterer hides its own shadow. Such backscattering reflectance features are exhibited by the bare soils measured by Kimes and Sellers (1985) and Milton and Webb (1987). Slight symptoms indication of forward scattering of the reflectance of ploughed fine-loamy texture soils was noticed by Irons and Smith (1990). The backscatter, as well as the forward scatter, regimes in soil reflectance were noticed by Deering et al. (1990). They demonstrated the phenomenon on examples of a flat bare alkaline soil and a dune sand surface, using a three-channel field radiometer working in the red, near-infrared and middle-infrared ranges. Laboratory results presented by Caulson (1966) show that desert soil materials like gypsum sand and quartz sand display a high reflectance with a strong forward scatter maximum in the visible and near-infrared ranges. These sands display maximum reflectance in the extreme forward scatter direction near the horizon. Shoshany (1993) collected more than 70 hemispherical data sets for different types of stony desert pavements and rocky surfaces in Australia under varied illumination conditions, using a apparatus for hemispherical

direction radiance measurements. He found that most of the surfaces exhibited an anisotropic reflection with a clear backscattering component.

The radiation environment of the above surfaces comprised of two hemispherical distributions of electromagnetic radiation, one incoming and one outgoing, has been frequently described by the bidirectional reflectance distribution function (BRDF), as defined by Nicodemus (1970). The function, best approached in practice by the measured biconical reflectance factor (BCRF), must obey the reciprocity theorem, i.e., the BRDF must not change, when the directions or cones of incidence and reflectance are exchanged (Kriebel, 1978). This unique feature of the BRDF is used to reduce to an acceptable level the number of measurements required to obtain the directional reflectance characteristics of a surface (Kriebel, 1996). The theoretical concept of the BRDF is described as the ratio of the radiance reflected by the surface to the incident irradiance from only one source of illumination. Similarly, with only one source of the incident radiation, another commonly used term, the bidirectional reflectance factor (BRF), is defined as the radiance reflected by the surface to the radiance which would be reflected by a perfect Lambertian

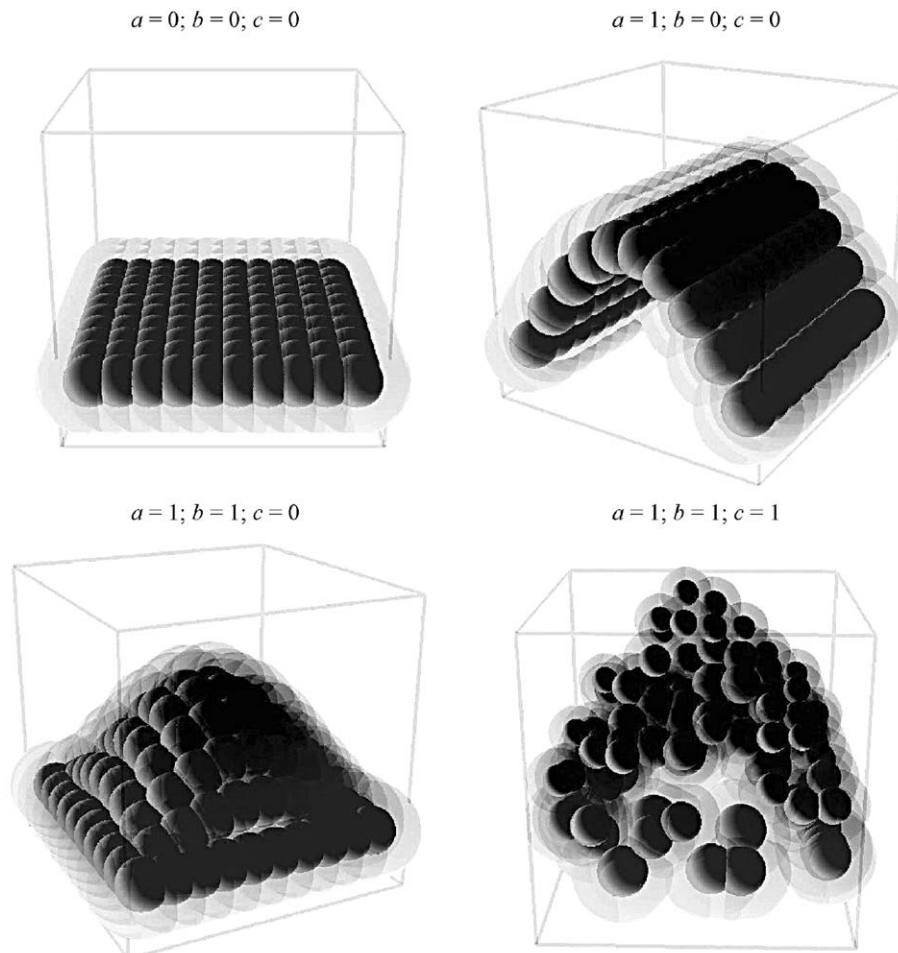


Fig. 1. Influence of the parameters a , b , and c on the shape of the R surface.

panel, both under the same illumination and viewing conditions (Milton, 1989). This constraint can be met under laboratory conditions, but only for surfaces containing small-scale structures. In field conditions, the limitation of only one source of radiation would mean an elimination of the diffuse sky radiation. This, of course, is unreal and therefore it is recommended that the directional reflectance measurements be taken on a day with a clear sky, under thin and stable aerosol conditions, and at wavelengths for which the sky radiance can be neglected (Sendmaier, 2000). Kriebel (1996) assumes that the measurements at wavelengths below $0.7 \mu\text{m}$ for vegetated surfaces, as well as for ploughed fields, can be performed with too large an error, because their reflectance is low and the atmospheric scattering is high. Sets of the directional reflectance measurements, related to a specific distribution of the sun and the sky irradiation, recorded at a specific time cannot be combined with the other sets taken at different times during the day in different atmospheric conditions. Abdou et al. (2000, 2001), Brugge et al. (2001), Strub et al. (2002, 2003), and Zhang et al. (2000) suggest that practical data about the directional reflectance behavior of different objects that have been collected so far, require the use of the hemispherical–directional reflectance factor, rather than the bidirectional reflectance approach, because the incident irradiance consist of a mixture of direct solar and non-isotropic diffuse illumination.

These difficulties in collection of BRDF data arouse interest in how they are modeled. Most geometrical soil

directional reflectance models have treated directly illuminated soil surface fragments as perfectly diffuse reflectors. The model by Norman et al. (1985) simulates soil aggregates using cuboids lying on a horizontal plane, and the model of Cooper and Smith (1985) describes soil surface irregularities by two microrelief forms whose height varies periodically with the cosine in one or two directions for ‘row’ and ‘clump’ soils, respectively. The soil surfaces in both the models are illuminated by just one point light source. In the model by Irons et al. (1992), direct as well as isotropically diffuse, light illuminates a surface made of uniform opaque spheres regularly spaced on a horizontal surface. The soil surface reflectance is expressed as a function of the horizontal area shaded by the spheres, the sunlit fraction, and the proportion of diffuse illumination, which depends on wavelength. All three models mentioned above exhibit clear backscatter reflectance features. Otterman’s model (1981) treats bare soil as thin vertical cylinders of variable heights with facet-reflectance and transmittance located randomly on a horizontal plane, also having Lambertian features. The model assumes that the facet-reflectance largely controls the backscatter, while facet transmittance is responsible for determining forward scattering. It is the first model to simulate both backscattering and forward scattering. The model by Cierniewski (1987, 1989) describes soil aggregates in terms of regularly spaced equal-sized opaque spheres lying on a freely sloping plane, illuminated only by direct beams. Its latest improved version (Cierniewski et al., 2002) considers a soil surface composed of equal-sized opaque spheroids of definite shape and size,

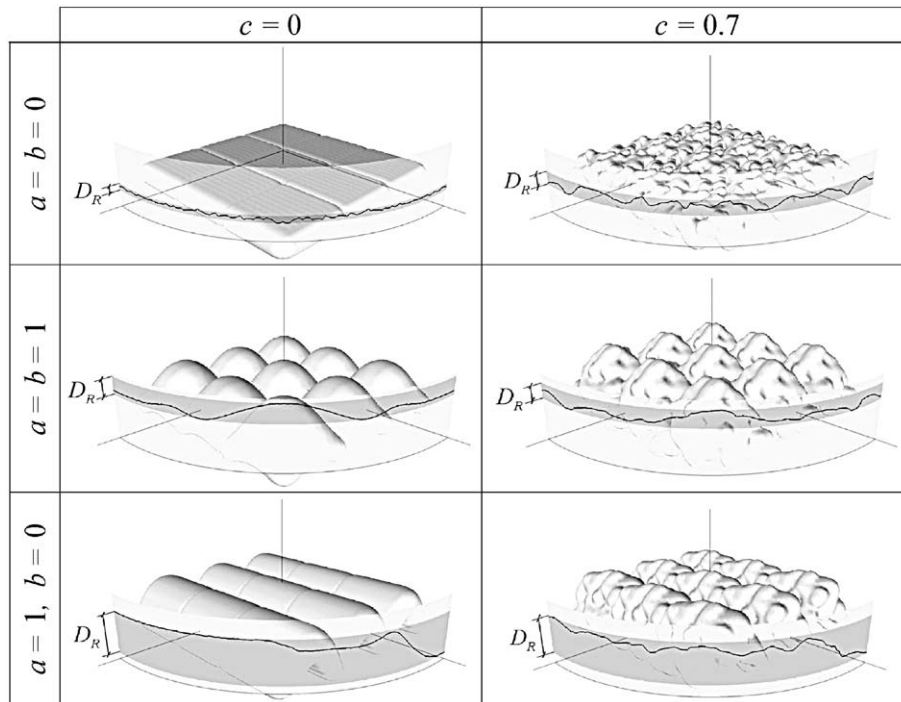


Fig. 2. Variation of the surface height deviation d_R in the ω angle function calculated over a segment of the length $2l$ along the direction ω and the surface shape directivity factor D_R for six soil surfaces generated with different values of the a , b , and c parameters.

dispersed in a net of squares on a freely sloping plane. They are absorbed into the plane; tops are at a height above it. Different values of the height, along and across the soil cultivation direction, are parameters, which express the variation of soil surface irregularities caused by furrowed farming treatments. The structure is illuminated by direct solar and diffuse light. Diffuse and specular wave energy is reflected from it. A sensor, suspended over the simulated soil surface, observes the surface at both a zenith and an azimuth angle in the forward scattering and backscattering directions. The reflectance from the rough soil surface is described by the normalized reflectance factor, which is

defined as the ratio of the total radiance measured from the off-nadir direction to the radiance measured from the nadir. The model was tested on the hemispherical/directional reflectance data collected under field conditions of ploughed and harrowed light soils in fresh farming treatments and after rain in Poland (Cierniewski, 2001), ploughed, harrowed and rolled heavy soils prepared for the colza sowing in France (Cierniewski et al., 2002), and uncultivated sandy and rocky soils in the Negev desert in Israel (Cierniewski & Karnieli, 2002).

This paper focuses on a presentation of a new directional reflectance model. The model describes in three-dimension-

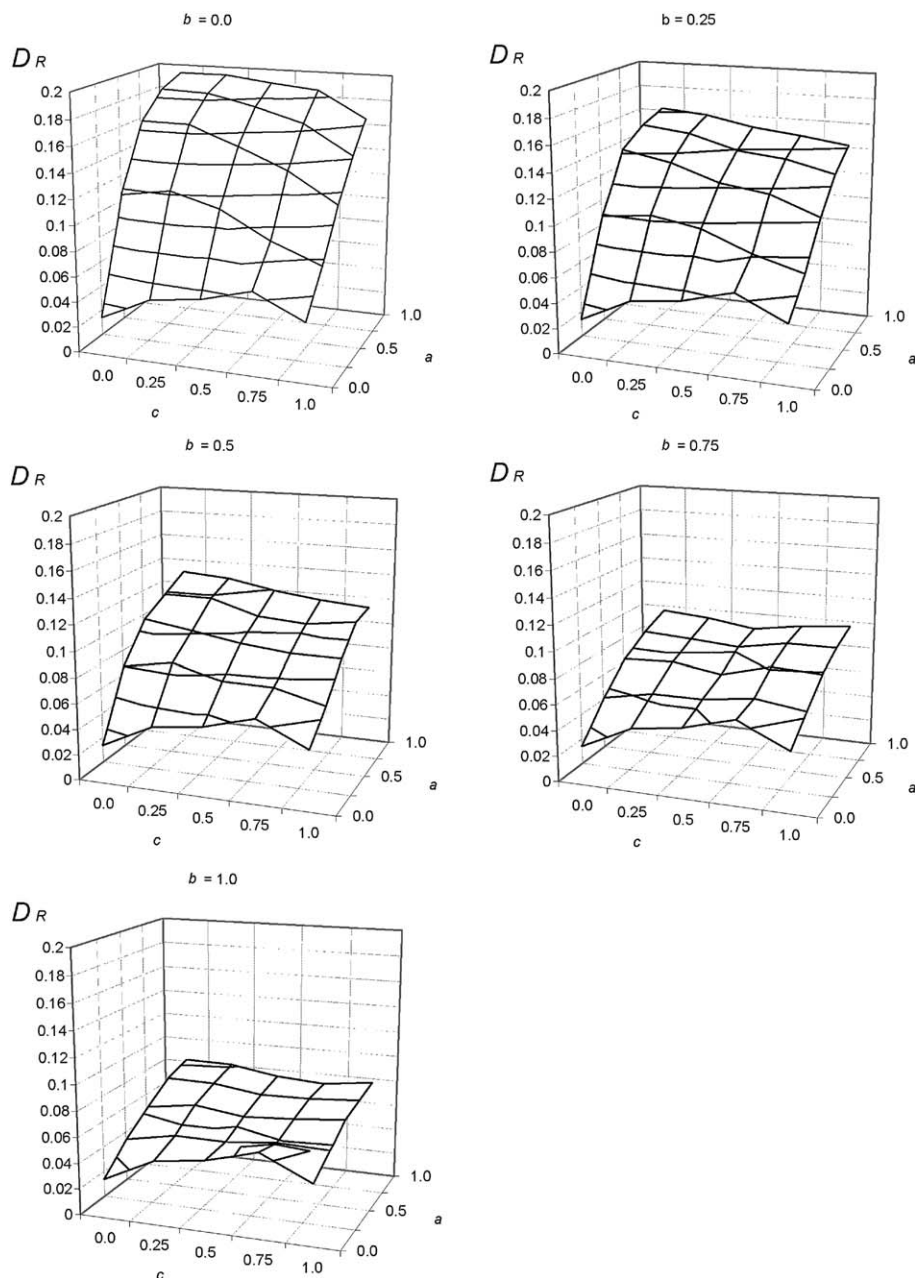


Fig. 3. Relationship between the surface shape directivity factor D_R and the geometrical parameters a , b , and c of soil surfaces generated by the model.

al space reflectance from rough surfaces in any direction as an effect of their illumination by an anisotropic–hemispherical light source, such as is found in outdoor conditions. The shape of soil surfaces is simulated by a geometrical structure more resembling real soil surfaces than structures used in the models mentioned above. Using the model, relating the anisotropic–hemispherical–directional reflectance and roughness directivities, the authors consider if it possible to detect the roughness directivity of a surface analyzing its hemispherical–directional reflectance. This study in the context of soil surfaces enable us to deeper understand image distinctions between cultivated soils with height irregularities of directional character that create a furrow microrelief, and uncultivated soils with their irregularities spread non-directly, randomly.

2. Methods

2.1. The model

Our model predicts the distribution of electromagnetic radiation reflected from an opaque rough surface. The R surface is constructed by means of a set of n points k_i of coordinates (x_i, y_i, z_i) of $i=1, \dots, n$ and the positive real numbers $r_1, r_2, r_3, \dots, r_n$ related to them, respectively. A pair (k_i, r_i) we can interpret as the sphere of radius r_i with the center k_i . The R surface is the solution of the following equation:

$$\sum_{i=1}^n (2d_i^3 - 3d_i^2 + 1) - \frac{1}{2} = 0, \tag{1}$$

where $d_i = \frac{\min(r_i, \sqrt{(x-x_i)^2 + (y-y_i)^2 + (z-z_i)^2})}{r_i}$. The R surface geometry is similar to that of the shape of beads merging into themselves. They either spread so far apart that there are gaps between them, or they penetrate each other.

For simplification, the centers k_i are dispersed regularly in the perpendicular projection to the XY plane, lying in a net of squares, each side $= 1/\sqrt{n}$, along the x and y axes. The height z_i of a sphere center k_i is expressed by the following equation:

$$z_i = a \cdot |\sin(\pi \cdot x_i)| \cdot \langle 1 - b \cdot [1 - |\sin(\pi \cdot y_i)|] \rangle + c \cdot f_{\text{dis}}(i), \tag{2}$$

where a describes the amplitude of the sinus function along the x -axis and b along the y -axis, relative to a . The final z_i position of a i th sphere is an effect of a disturbance approximated by the sequence $f_{\text{dis}}(i) \in [0, 1)$ with uniform distribution. The c describes the maximum deviation from the z_i value, as determined by only the a and b parameters. The radii r_i of the spheres used for

construction of the R surface fragments change according to the following formula:

$$r_i = [3 - c \cdot f_{\text{dis}}(i)] \frac{1}{\sqrt{n}}, \tag{3}$$

and matched to the r_i values of the spheres to eliminate the gaps between them after their deformation. Fig. 1 shows the influence of the a , b , and c amplitudes on the shape of the R surface.

The model assumes that the average height $\tilde{f}(\omega)$ of the R surface top, the height described by the function $f(x, y) = \max_z R(x, y, z)$, calculated over a segment of the length $2l$ along the direction defined by an ω angle, is expressed by the formula:

$$\tilde{f}(\omega) = \frac{1}{2l} \int_{-l}^l f(t \cos(\omega), t \sin(\omega)) dt. \tag{4}$$

The deviation of this height $d_R(\omega)$ is expressed by the equation:

$$d_R(\omega) = \frac{1}{2l} \sqrt{\int_{-l}^l (\tilde{f}(\omega) - f(t \cos(\omega), t \sin(\omega)))^2 dt}. \tag{5}$$

The directivity factor D_R of that surface shape is defined as follows:

$$D_R = \min_{(x_0, y_0)} (\max_{\omega} d_R(\omega) - \min_{\omega} d_R(\omega)), \tag{6}$$

using the maximum and the minimum values of the $d_R(\omega)$. Employing the d_R and D_R parameters as tools for evaluation of the directional features of the R surface height irregular-

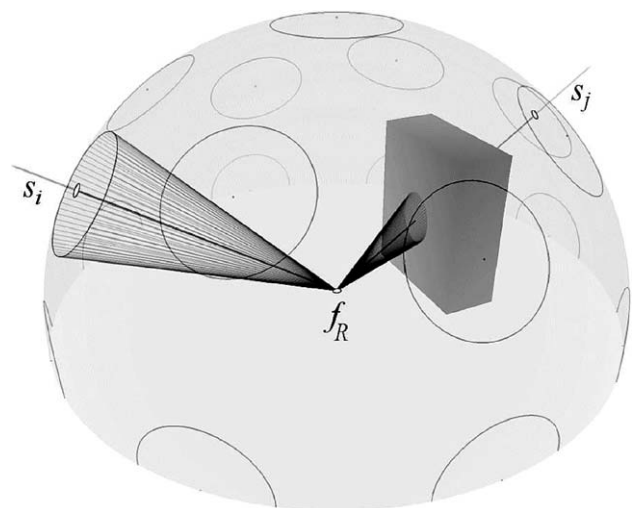


Fig. 4. Effects of illumination of an elementary fragment f_R of the surface R by two of m point light sources equally distributed on the hemisphere. Their energy can come directly to the f_R fragment, as from the s_j source, or cannot approach the f_R being blocked by an adjoining part of the R, as from the s_i source.

ities is explained in Fig. 2, using as examples six soil surfaces with varying geometry. The distinctness of these surfaces' shape directivity D_R rises with the increase of their a value and the decrease of their b value. The influence of the geometrical parameters a , b , and c on factor D_R , presented in Fig. 3; the range between 0 and 1 at 0.25 increments was used for all these geometrical parameters. The higher the a and the lower the b , that is, the deeper and more distinct the furrows, the larger D_R becomes. The influence of the disturbance parameter c on the D_R is much weaker than those of a and b , and is ambiguous. For sufficiently clearly shaped furrows, described by the $a \geq 0.25$ and the $b \leq 0.5$, an increase in c enhances a decrease in the D_R . However, for surfaces with insufficiently prominent furrows, this relation

between the D_R and the c is reversed, i.e., a decrease of the D_R results from a decrease in c .

The opaque R surface is illuminated by a hemisphere light source H :

$$H = \{(s_1, e_1), (s_2, e_2), \dots, (s_m, e_m)\}, \tag{7}$$

created by a number m of point sources $s_1, s_2, s_3, \dots, s_m$ of the intensity $e_1, e_2, e_3, \dots, e_m$, respectively, equally spread on the hemisphere (Fig. 4). Irregularities on the R surface will make it impossible to completely illuminate it by all of the m point sources on the hemisphere. A part of the light coming from these point sources s_i along the directions \vec{s}_i to an elementary fragment f_R of the R surface can be blocked by the presence of adjoining fragments of the R surface.

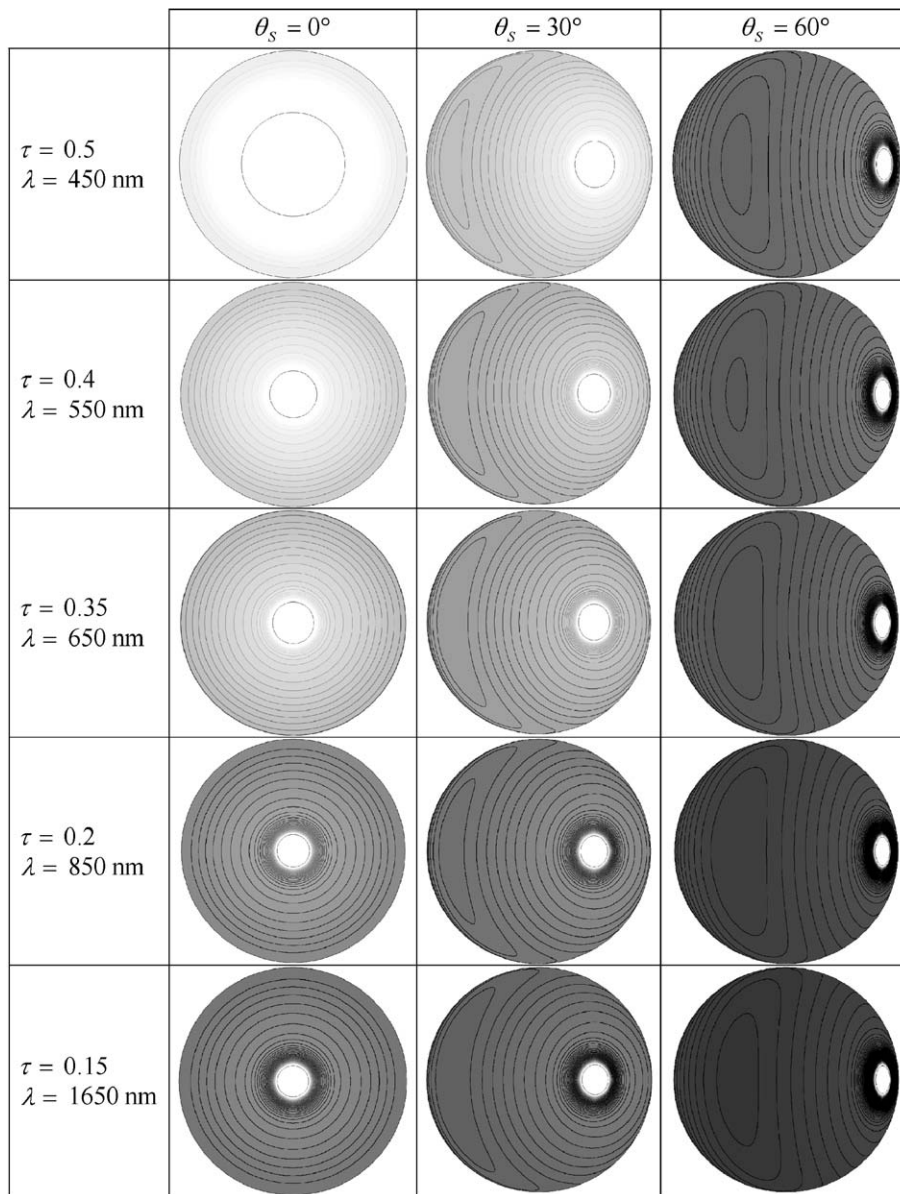


Fig. 5. Distributions of the hemispherical light for the non-absorbing Rayleigh atmosphere depending on the solar zenith angle θ_s and the normal optical thickness τ attributed to the wavelength λ . The relationship between τ and λ was obtained from Fraser (1975).

When the model is applied to outdoor conditions, it is assumed that the ratio of the direct solar irradiance to the global irradiance $\delta(\vec{S}, \tau)$ for clear sky conditions changes with the sun's position $\vec{S} = [\theta_S, \phi_S]$ and the normal optical thickness τ . Fig. 5 shows the distributions of the hemispherical light for the non-absorbing Rayleigh atmosphere, dependent on the zenithal position of the sun θ_S and the normal optical thickness τ attributed to the wavelength λ . The intensity of the direct solar irradiance at point S reaches 1 independent of both τ and λ . τ enables us to control in a flexible manner the contrast between shaded and sunlit fragments of the studied surfaces, taking into account the wavelengths and quality and content of aerosols in the atmosphere (Fraser, 1975). Distribution of the hemispherical light energy $H_{\vec{k}}$ along a \vec{k} direction is described in the model by the following formula:

$$H_{\vec{k}} = c_1 + c_2(\angle(\vec{k}, \vec{n}_d))^2 + g \cdot e^{c_3 \cdot \angle(\vec{S}, \vec{k})} + c_4 \cdot \cos^2(\angle(\vec{S}, \vec{k})), \tag{8}$$

where \vec{n}_d is the nadir, and $c_1, c_2, c_3,$ and c_4 are the constants, such as in the equation of Grant et al. (1996). c_1 is the minimum amount of the hemispherical light energy, c_2 describes an amplification of the energy near the horizon, c_3 is the measure of the concentration of the solar aureole near the point S , and the c_4 describes the energy at the darkest part of the hemisphere light (in the quadrant opposite the sun). g is the variable describing the amount

of the light energy coming directly from the sun, satisfying the following equation:

$$\delta(\vec{S}, \tau) = \frac{H_S}{H_G}(\vec{S}, g), \tag{9}$$

where H_S is the direct solar irradiance used in the distribution of the $H_{\vec{k}}$ and H_G is the global irradiance for clear sky conditions. Finally, the light energy coming from s_i is defined as:

$$e_i = \frac{H_{s_i}}{g}. \tag{10}$$

The shape of the opaque soil surface R, described by Eq. (1), enable us to define the vectors of the normal to this surface at any point necessary in order to express the amount and the direction of reflected energy from total area of the R. The beam energy $e_{f_R}(i, \vec{k})$ reflected only once from the fragment f_R along the direction \vec{k} , due to illumination from the unblocked point source, s_i , given as:

$$e_{f_R}(i, \vec{k}) = e_i \cdot f(\vec{s}_i, \vec{n}, \vec{k}), \tag{11}$$

where \vec{n} is the normal to the fragment f_R .

A set of all of the vectors $\vec{k} \cdot e_{f_R}(i, \vec{k})$ creates a cloud of a specified shape and size in the 3D space, characterizing the scattering properties of the R surface for its elementary fragments f_R . The total light energy $E(f_R, \vec{v}, H)$ reflected from the fragments f_R in the direction \vec{k} and

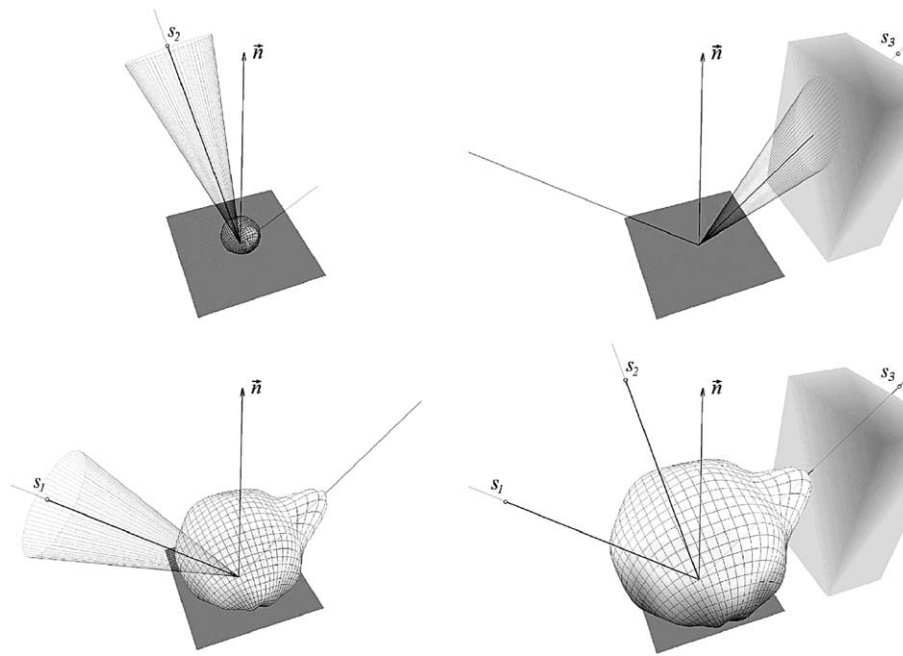


Fig. 6. Distribution of light energy, coming from sources s_1 and s_2 of the intensity $e_1 > e_2$, respectively, reflected from an elementary fragment f_R of the R surface. The energy coming from the s_3 source, being covered by an adjoining fragment of the R, does not reach the f_R and therefore it is not taken into account for the final energy distribution, as in the lower right part of the figure.

viewed by the sensor along a direction $\vec{v} = [\theta_v, \phi_v]$ is given by:

$$E(f_R, \vec{v}, H) = \sum_{i=1}^m e_{f_R}(i, \vec{v}), \quad (12)$$

where the sum is limited only for the unblocked light sources s_i (Fig. 6). Similarly, the function HDRDF(R, \vec{v}, H):

$$\text{HDRDF}(R, \vec{v}, H) = \frac{1}{|\Omega|} \int_{\Omega} E(R, \vec{v}, H) d\Omega \quad (13)$$

describes the hemispherical–directional reflectance of the whole surface R , where Ω is the field of view of a sensor suspended over the surface.

The model assumes that effects of viewing the R surface depend on illumination by the hemisphere light, as well as on the scattering features at its elementary points. Fig. 7 presents the brightness variation of a surface, viewed from the same directions as the effect of the hemispherical light scattering, according to the following four selected functions, describing the beam energy reflected from its elementary fragments:

- The simplest theoretical scattering function:

$$f_1(\vec{s}_i, \vec{n}, \vec{k}) = 1, \quad (14)$$

considers an impossible effect, when the scatter is independent of the incidence angle from each of the point hemisphere light source. So, it only expresses the distribution of the hemisphere light energy that is able to reach given fragments of the surface. As the consequence, the tops of the surface are brighter than its bottom parts, surrounded by other surface fragments that partially block the hemisphere energy.

- The Lambertian scattering function:

$$f_2(\vec{s}_i, \vec{n}, \vec{k}) = \max(0, \cos \angle(\vec{s}_i, \vec{n})), \quad (15)$$

causes the distribution of the reflected energy from a given fragment of the surface, with dependence upon the incidence angle of the energy coming to the fragment with respect to the normal.

- The quasi-specular scattering properties are described by the function:

$$f_3(\vec{s}_i, \vec{n}, \vec{k}) = \max(0, \cos \angle(\vec{k}, 2 \cdot (\vec{s}_i \circ \vec{n}) \cdot \vec{n} - \vec{s}_i))^\alpha, \quad (16)$$

where the constant α is a positive number, expressing the concentration of the specular component along the direction determined by the angle of reflection equal to the incidence angle. Eq. (15) generates the distribution of the reflected energy dependent upon the incidence angle of the energy

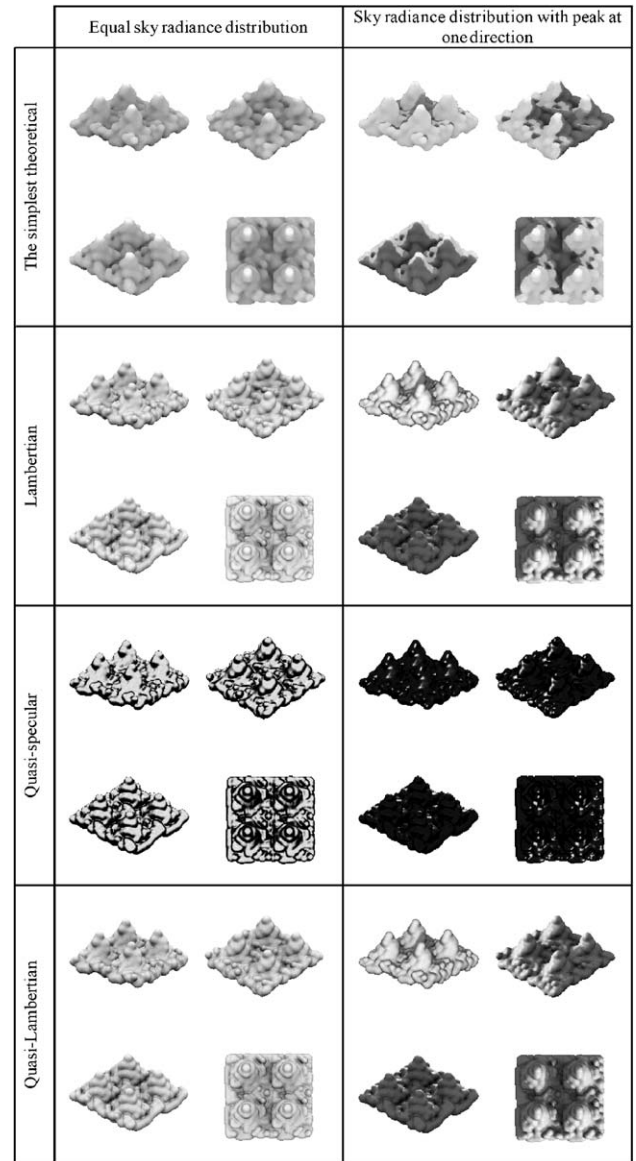


Fig. 7. Brightness variation of a surfaces R , scattering light energy according to the four-selected reflectance function and viewed along the same directions. At the left column, the R surface is equally illuminated by the hemisphere light sources of the same intensity; however, at the right column, the R is unequally illuminated by one source with the dominant intensity to others.

coming to the fragment with respect to its normal, as well as on the angle of viewing of the reflected energy.

- The effect of the quasi-Lambertian scattering features, expressed by the function:

$$f_4(\vec{s}_i, \vec{n}, \vec{k}) = f_2 + (1 - f_2) \cdot f_3, \quad (17)$$

indicates a real effect of viewing the surface, as a combination of the Lambertian scattering (Eq. (15)) and the quasi-specular scattering functions (Eq. (16)).

It was also assumed that the hemispherical–directional reflectance function HDRDF of soil surfaces of a given

geometry not only includes general information about surface shape, i.e., that it is more or less rough, but it also contains further details, such as the directivity of the surface shape. It was found that information about the directivity of soil surface geometry can be obtained by analyzing the symmetry of the HDRDF with respect to the solar principal plane (SPP). The HDRDF function of surfaces, with an indirect, random spread of their height irregularities, is almost symmetrical. However, the HDRDF of surfaces with directional microrelief-like furrows has been shown to be asymmetrical: the greater the asymmetry, the stronger the directional character of the surfaces. The absolute difference in the R surface reflectance Δ_{HDRDF} , viewed from two directions, is described by the same value of the zenith view angle θ_v , but by different values of the horizontal view angle in relation to the SPP, $+\phi_v$ and $-\phi_v$ expressed as:

$$\Delta_{\text{HDRDF}}(\theta_s, \phi_s, \theta_v, \phi_v) = |\text{HDRDF}(\theta_s, \phi_s, \theta_v, \phi_s + \phi_v) - \text{HDRDF}(\theta_s, \phi_s, \theta_v, \phi_s - \phi_v)|, \quad (18)$$

which is an elementary component of the asymmetrical features of the HDRDF. A set of cylinders of height Δ_{HDRDF} represents this asymmetry in Fig. 8 for a given illumination condition, described by the solar zenith angle

θ_s and the solar horizontal angle ϕ_s . The maximum height of the cylinder $d_{\text{HDRDF}}(\theta_s, \phi_{c-s})$ inside a set defined as:

$$d_{\text{HDRDF}}(\theta_s, \phi_{c-s}) = \max_{\theta_v, \phi_v} \Delta_{\text{HDRDF}}(\theta_s, \phi_{c-s}, \theta_v, \phi_v), \quad (19)$$

was calculated for the surfaces characterized by the geometrical parameters $a=1, b=0, c=0.7$, illuminated under the constant solar zenith angle $\theta_s=70^\circ$ with changing solar horizontal angles ϕ_s from 0° to 75° under clear sky conditions for a thickness $\tau=0.15$, which approximates the wavelength of 1650 nm for the non-absorbing Rayleigh atmosphere. The angle $\phi_s=0^\circ$ describes a situation in which the sunbeams reach the surface along the direction of the surface furrows. Finally, the directivity factor of the surface hemispherical–directional reflectance function D_{DRDF} is expressed in the formula:

$$D_{\text{HDRDF}} = \max_{\theta_s} (\max_{\phi_s} d_{\text{HDRDF}}(\theta_s, \phi_{c-s}) - \min_{\phi_s} d_{\text{HDRDF}}(\theta_s, \phi_{c-s})). \quad (20)$$

The influence of a, b , and c on the factor D_{HDRDF} , presented in Fig. 9, relates to clear sky conditions for the

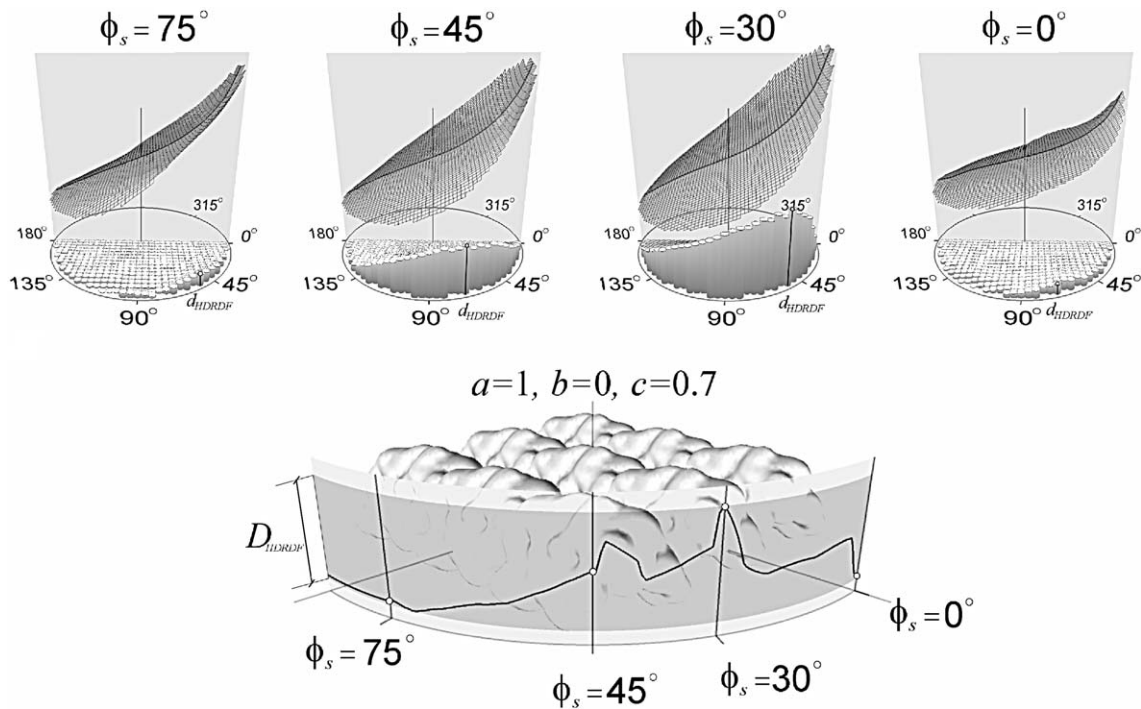


Fig. 8. Shape of the hemispherical–directional reflectance function HDRDF of the chosen furrowed surface (characterized by the a, b , and c parameters), illuminated at the constant solar zenith angle θ_s equal 70° and the changing solar horizontal angle ϕ_s from 0° to 75° in clear sky conditions for wavelength of 1650 nm; below variation of the HDRDF differences Δ_{HDRDF} calculated for pairs of view directions symmetrical to the solar principal plane (gray plane) with marked its maximum values d_{HDRDF} for changing ϕ_s ; at the bottom of the graph is variation of the d_{HDRDF} in the ϕ_s function and the final value of the directivity factor D_{HDRDF} of the HDRDF for the analyzed surface.

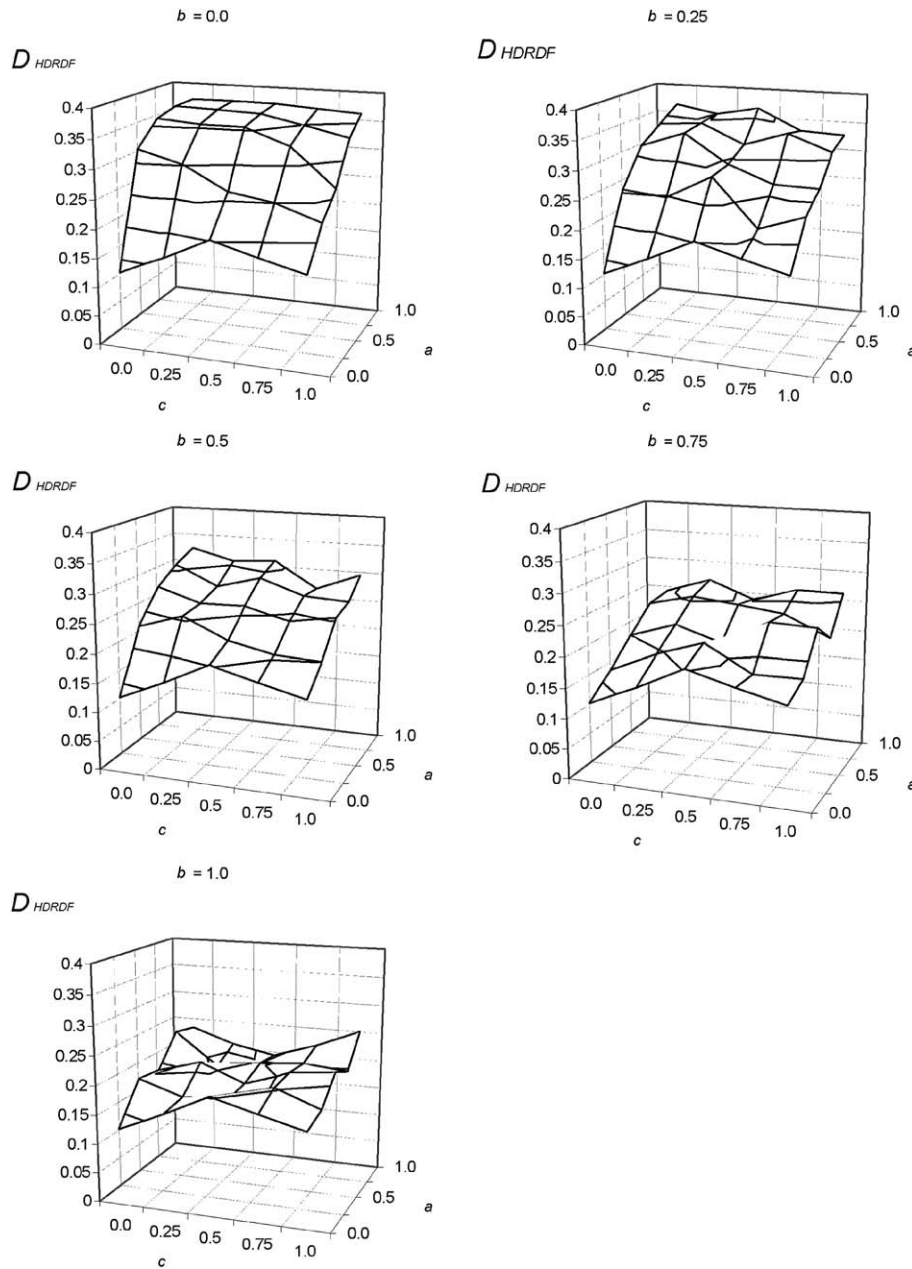


Fig. 9. Relationship between the geometrical parameters a , b , and c of simulated surfaces and the directivity factor D_{HDRDF} .

wavelength of 850 nm with $\tau=0.2$ and the solar zenith angle θ_S varying from 0° to 70° . This aspect was studied in the same range and increments of a , b , and c as in the relationship to the directivity factor of soil surface geometry D_R (Fig. 3), i.e., between 0 and 1 at 0.25 increments. This relationship between these geometrical factors and the D_{HDRDF} resembles their relationship to D_R . The higher a and the lower b , the larger D_{HDRDF} . The influence of c on D_{HDRDF} is also much weaker and hazier.

Data generated in the following procedure were used to check for a potentially precise description of the relationship between the directivity factor of soil surface

geometry D_R and the directivity factor of the reflectance function D_{HDRDF} . At first, many different combinations of the geometrical parameters a , b , and c were specified, which provided sufficient detail in order to represent many possible variations of soil surface geometry. These combinations, 125 in number, were created using 5 different values for each of the parameters, expressed by numbers between 0 and 1, in 0.25 increments. Then, for each of these abc combinations, the values of the D_R and the D_{HDRDF} factors were calculated using Eqs. (6) and (20), respectively. All values of these D_R and D_{HDRDF} factors are presented in

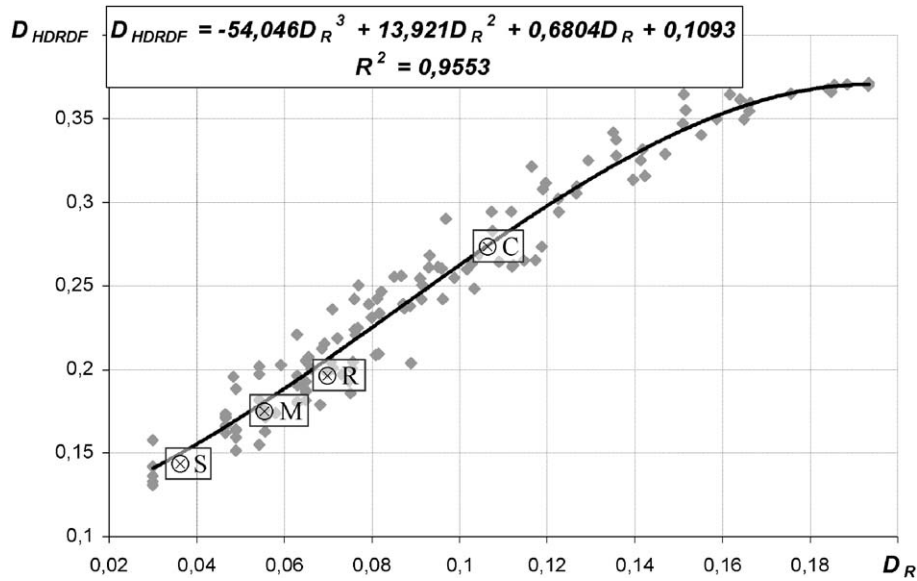


Fig. 10. Relationship between the directivity factor of soil surface shape D_R and the directivity factor of the hemispherical–directional reflectance distribution function D_{HDRDF} . Marked dots: S, M, R, and C describe this relationship for the uncultivated smooth, moderate, rough surfaces, and the cultivated surface with furrows, respectively.

Fig. 10; a high correlation between them, expressed by the coefficient of determination r^2 higher than 95% can be noted.

2.2. Test surfaces

The model was tested on one cultivated and three uncultivated surfaces in Israel. The cultivated surface, situated in a field of an experimental agricultural farm near Beer-Sheva (31.33°N, 34.67°E), was specially prepared. In order to more easily detect directional features of the hemispherical–directional soil reflectance, the most

beneficial orientation of the field furrow direction was predicted by the model discussed above. The three uncultivated surfaces are located in the Negev desert, one, a silty surface, near Sede Boker (30.84°N, 34.78°E) and two others, rocky surfaces, at Makhtesh Ramon (30.36°N, 34.50°E).

2.3. Directional reflectance measurements

The hemispherical–directional reflectance features of these surfaces were measured by a five-channel field radiometer CIMEL 313-21. The instrument, with a 10° field of

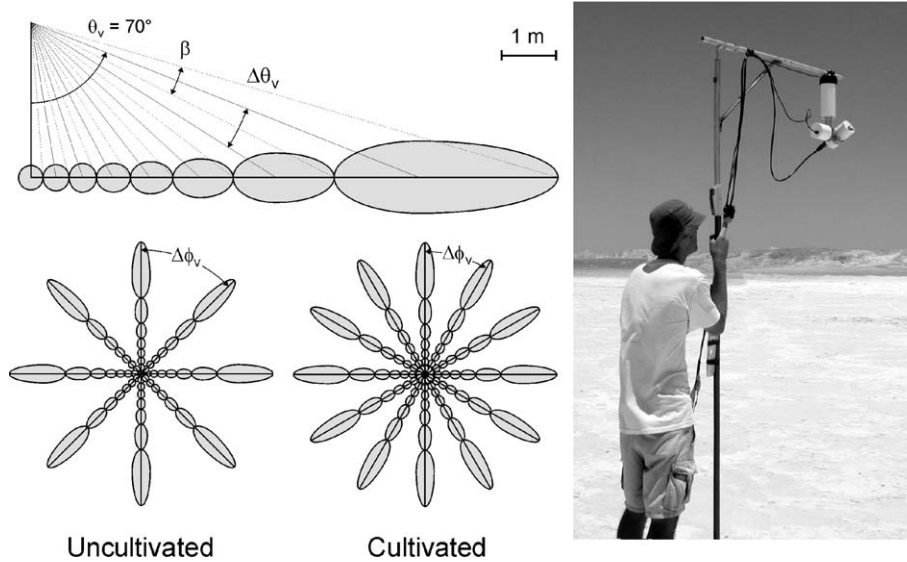


Fig. 11. Field radiometer CIMEL 313-21 and its viewing schema along a half of a measurement plane with the location of measurement planes on the tested surfaces.

view β , records the radiance of a target in the following spectral bands: 450, 550, 650, 850 and 1650 nm. The instrument collected the radiance data along the SPP, as well as several other planes situated in relation to the sun's direction at 30° increments of the view horizontal angle $\Delta\phi_v$ for the cultivated surface and at the increments of 45° for the uncultivated surfaces. The radiance was measured at each plane at 15 view zenith angles θ_v from -70° (forward, towards the sun), through the nadir (0°) to $+70^\circ$ (backward, away from the sun) at 10° increments $\Delta\theta_v$. Additionally, nadir measurements were conducted at the beginning and at the end of each sequence, thus their total number in each plane was 17. The instrument, setting up on a goniometric support 2.6 m above the target, enabled us to collect the data for a horizontal surface from the circle sample area of 0.162 m^2 for the nadir and from the elliptical area of 1.475 m^2 for the oblique view at the θ_v equals 70° (Fig. 11). The radiometer collected the radiance data automatically, changing the horizontal ϕ_v and the zenith θ_v angles, focusing on fragments of the measured surfaces that were progressively farther away. The radiance measurements in one plane consumed 2 min for all the spectral bands. All reflectance measurements were recorded under clear sky conditions.

3. Results and discussion

3.1. The tested surfaces

The view all of the tested surfaces is presented with their virtual equivalents in Fig. 12. The cultivated soil surface situated in a field of an experimental agricultural farm was prepared by a cultivator. Very dry material of the studied soil (*Calcic Xerosol* according to the FAO soil classification), developed from sandy loam with 0.6% of organic matter content and 16% of CaCO_3 content in the surface horizon, enabled us to create fairly shallow furrows with the average depth of 10 cm. The distance between each successive top was 60 cm. A simulation of the hemispherical-directional reflectance distribution function HDRDF of the furrowed surface, made before the measuring experiment, suggested to us that we orient the direction of the furrows in relation to the sunbeams ϕ_{c-s} , with an angle of between 30° and 45° . Knowing that the asymmetry of the HDRDF is easiest to detect at a high solar zenith angle θ_s , we planned to orient the furrows at 65° to the geographic North. All the tested surfaces, the cultivated and the uncultivated ones, were chosen as homogeneous in terms of roughness within the entire radiometer field of view, i.e., in the circle of the minimum 20 m diameter.

3.2. Directional reflectance features of the studied surfaces

The radiance data of the cultivated surface with furrows (C) were collected on July 14, 2003 for six values of the

solar zenith angles θ_s , varying from 34.2° to 80.0° . They were recorded only for four channels of wavelengths 550, 650, 850 and 1650 nm. The measurements of the uncultivated surfaces were carried out on July 12, 2001 in Sede Boker, Israel, at solar zenith angles θ_s , ranging from 9.1° to 75.6° for the silt surface (S), and on July 19 and July 26, 2001 in Makhtesh Ramon, at solar zenith angles θ_s , ranging from 9.4° to 76.6° for the moderately rough rocky surface (M) and from 10.9° to 76.8° for the very rough surface (R), respectively. All the data for uncultivated surfaces were recorded in 14 series for solar zenith angles θ_s , also changing in approximately 5° increments. The errors in the reflectance data that were collected in those measuring experiments do not exceed 0.11 (Cierniewski, 2001).

The measured reflectance data of the tested surfaces are presented in Fig. 13a in the form of a 3D graphs for several chosen illumination conditions, defined by the solar zenith angle θ_s and additionally by the angle ϕ_{c-s} describing illumination of the furrows for the cultivated surface. The graphs for the measured data are plotted against the data generated by the model for the same illumination conditions (Fig. 13b). These graphs show the distribution of the hemispherical-directional reflectance function of these surfaces in the function of their zenith angle view θ_v and horizontal angle view ϕ_v , normalized to the nadir viewing. Variation of the θ_v is marked by concentric circles surrounding the nadir at 10° increments spread on the top of the graph. The central point of the distribution describes the $\theta_v=0^\circ$ (the nadir viewing), while the most exterior circle, describes $\theta_v=70^\circ$. Other lines on the graph describe the distribution of the reflectance data for different solar zenith angles θ_s and angles ϕ_{c-s} .

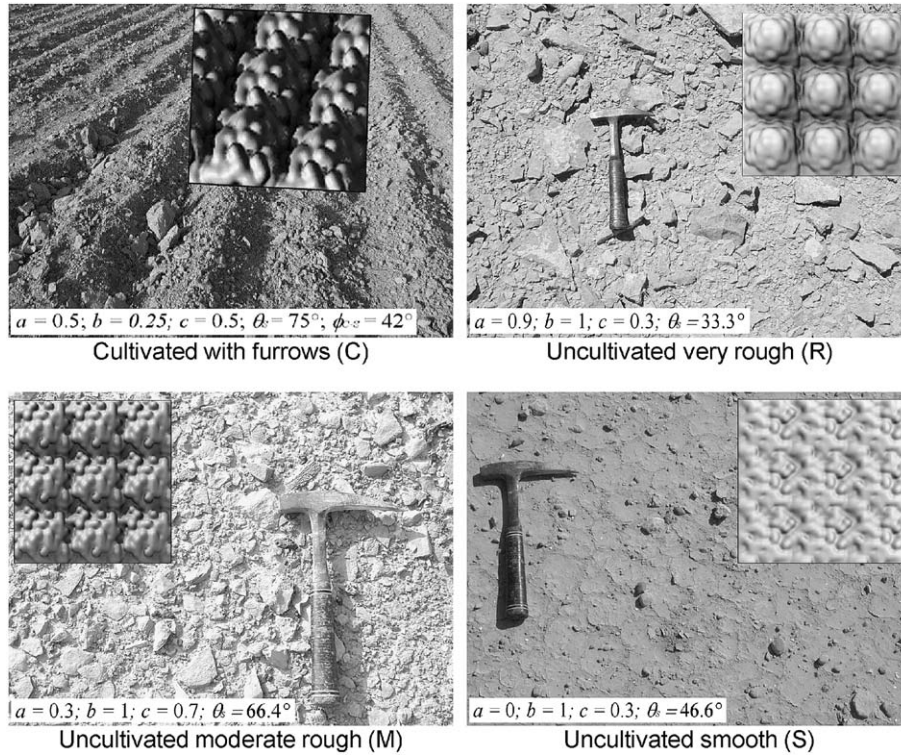


Fig. 12. View of the tested soil surfaces, the cultivated (C) and the uncultivated: relatively smooth (S), moderate rough (M), and rough (R), recorded at visible range with their virtual equivalents generated for the red wavelength at the same geometry of their illumination and viewing.

hemispherical–directional reflectance. The virtual surface, being the set of three geometrical parameters describing the shape of a studied surface, functions in the model as a part of the input data necessary to predict the surface’s directional/anisotropic–hemispherical reflectance. Two of these parameters, a and b , express the height irregularities of the surfaces along the x and y axes, respectively, using the sinus function. The third parameter, c , defines the disturbance in these irregularities. In fact, this function determines a class of the irregularities shape. It was chosen to the model as a possible simple function, which also enable us to generate soil surfaces with different directivity. The model presented above assumes that the set of the geometrical parameters a , b , and c is independent of the illumination and viewing conditions for a given surface. This assumption was taken into account when formulating the procedure for fitting these parameters to the hemispherical–reflectance data related to the surface. This procedure involves choosing those values of the virtual surface parameters, a , b , and c , which give the lowest possible root mean square error rms between the measured and the modeling reflectance data for all the wavelength bands used:

$$\text{rms} = \min \left(\sum_{n=1}^n \frac{1}{n-1} \sqrt{\sum_{n_v=1}^{n_v} (M_{\theta_s, \phi_s, \theta_v, \phi_v, \phi_c} - P_{\theta_s, \phi_s, \theta_v, \phi_v, \phi_c, s})^2} \right), \quad (21)$$

where n_v is the number of the analyzed radiance data, $M_{\theta_s, \phi_s, \theta_v, \phi_v, \phi_c}$ is the measured value of radiance for given angles θ_s , ϕ_s , θ_v , ϕ_v and ϕ_c , $P_{\theta_s, \phi_s, \theta_v, \phi_v, \phi_c, s}$ is the predicted value of radiance for these angles, and the set s of parameters: a , b , c . Finally, the minimum value of the rms indicates the set s for which the average mean square root is the lowest. Generating the hemispherical–directional reflectance for all of the virtual surfaces that the following assumptions and decisions were made:

- the number n of spheres inside that virtual surface R is $40 \times 40 = 1600$;
- the number of the individual point light sources m in the hemispherical light for each of the wavelengths is 297;
- the virtual surface is illuminated as for a clear sky, using Eq. (8) with the following values of its constants: $c_1 = 0.201$, $c_2 = 0.02$, $c_3 = -7.8$, $c_4 = 0.148$, as in the paper of Grant et al. (1996);
- scattering of the surface is quasi-Lambertian, characterized by a constant expressing the concentration of the specular component along the main direction of reflection $\alpha = 6$;
- values of the geometrical parameter a , b , and c were fitted with the precision of 0.1;
- other parameters describing conditions of illumination and observation of the studied surfaces, θ_s , ϕ_s , θ_v , and ϕ_v , were taken as their measured values.

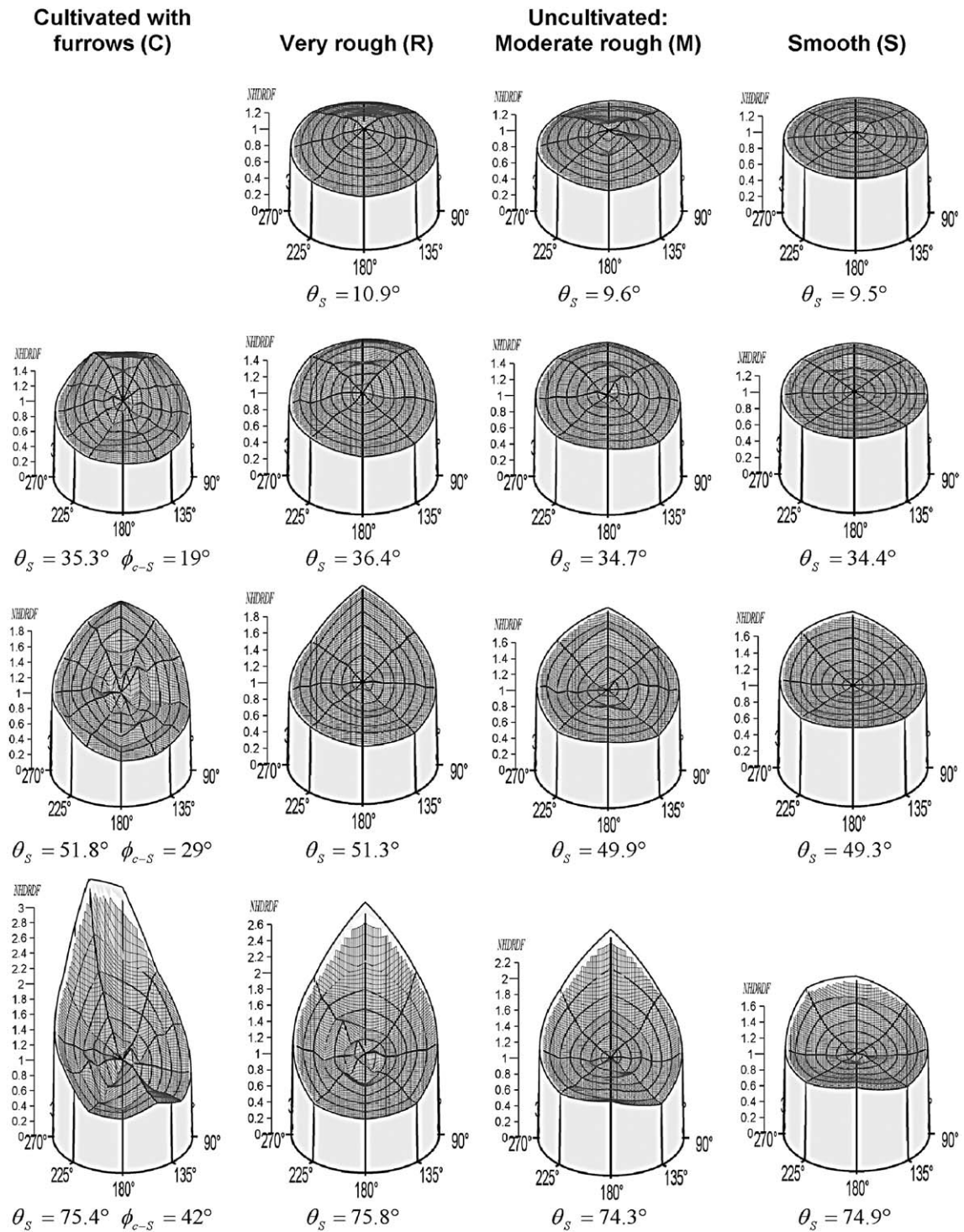


Fig. 13. (a) Distributions of the normalized hemispherical–directional reflectance function NHDRDF of the tested surfaces obtained from the measured data for the wavelengths of 850 nm for chosen illumination conditions defined by the solar zenith angle θ_s and additionally by the angle ϕ_{c-s} describing illumination of the furrows as a distance angle between the direction of the furrows and the sun position. (b) Distributions of the normalized hemispherical–directional reflectance function NHDRDF of the tested surfaces predicted by the model for the wavelengths of 850 nm for chosen illumination conditions defined by the solar zenith angle θ_s and additionally by the angle ϕ_{c-s} describing illumination of the furrows as a distance angle between the direction of the furrows and the sun position.

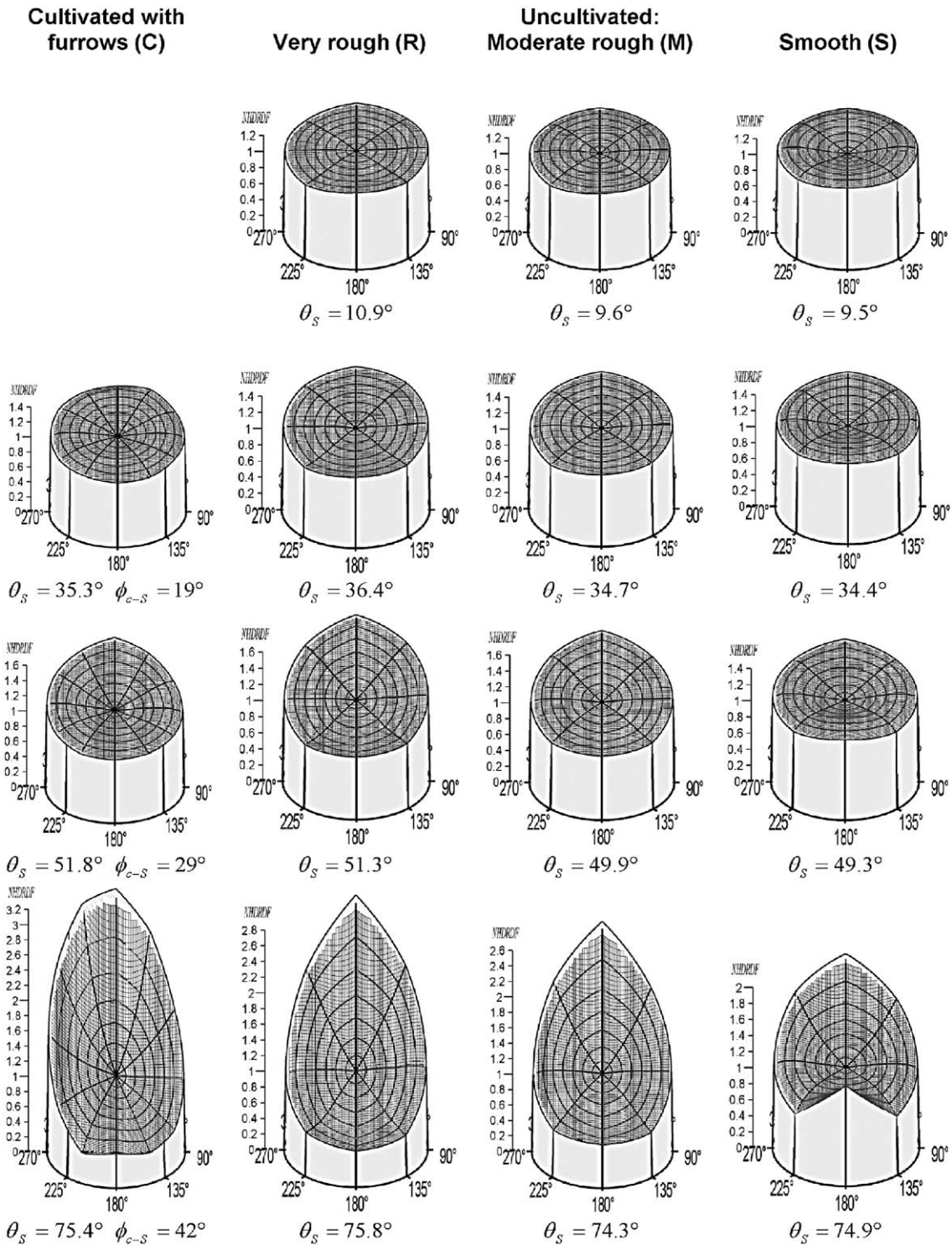


Fig. 13 (continued).

The virtual surfaces were obtained using the radiance data for each of the wavelengths used with n_v equal to 270 and 780 for the cultivated surface with furrows and for the uncultivated surfaces, respectively.

The accuracy of the virtual surface fit was assessed using the mean square root error rms calculated for each of

the wavelengths (four for the cultivated and five for the uncultivated) and for the total set of the reflectance data collected for the given surfaces at all of the wavelengths together (Table 1). The accuracy for the furrowed soil surface (C) is lower than that for the uncultivated surfaces. The highest accuracy was obtained for the relatively

Table 1
Root mean square error rms calculated for measured and generated by the model NHDRF data for the tested surface

Surfaces	450	550	650	850	1650	All
	nm	nm	nm	nm	nm	wave
rms						
Cultivated with furrows	–	0.142	0.135	0.120	0.111	0.132
Uncultivated very rough	0.130	0.102	0.110	0.092	0.102	0.100
Uncultivated moderate rough	0.101	0.091	0.085	0.080	0.072	0.080
Uncultivated relatively smooth	0.101	0.080	0.066	0.063	0.058	0.072

smooth silt surface (S). The data of the uncultivated surfaces clearly shows the longer the wavelength, the higher their accuracy.

The distributions of the mean square root error rms in the function of the a and c parameters enable us also to assess the sensitivity of the procedure with respect to these parameters for the wavelength of 850 nm and all the measured wavelengths, separately (Fig. 14). Both groups of rms distributions are very similar. Neither flattens with respect to a and c , and thus these geometric parameters are available to match in this procedure. The shaded areas, marking the combinations of the parameters which were recovered with near the same values of the rms like its minimum, relating to the best fitted set of the parameters, show that the analyzed surfaces, despite their different shape, can characterize very similar hemispherical-directional reflectance. This effect, mentioned also by Shoshany (1991) as the equifinality of the bidirectional reflectance distribution, is observed for the studied surfaces at different variation range of the geometrical parameters a and c . The equifinality is especially visible for the uncultivated moderate rough surface (M), where it can be observed in the widest range of the a variation, as well as the parameter c .

The virtual surfaces used in this procedure as the set of geometric parameters a , b , and c look similar to their real equivalents, especially when they are seen under the same illumination and viewing conditions under which the images of the real surfaces were recorded (Fig. 12). The virtual surfaces of the tested surfaces have a similar character to the real ones, e.g., the virtual surface of the cultivated surface (C) has furrows, and the uncultivated surfaces do not have them. The shape of these furrows is described by the parameter $0 < b < 1$, and when they are absent, the parameter is $b = 1$. Furthermore, the greater the roughness of the real surfaces, the greater that of their virtual equivalents. Weak irregularities of the smooth surface (S) were treated as an ideal flat surface, characterized by $a = 0$ and $b = 1$, deformed only by the disturbance parameter $c = 0.3$. The higher irregularities of the virtual creations corresponding to the two uncultivated surfaces with higher roughness levels, i.e., the moderately rough (M) and the very rough (R) surfaces, are simulated with a relatively low value of the parameter

$a = 0.3$ and a high value of $c = 0.7$ for the M surface, and conversely, with a high $a = 0.9$ and a low $c = 0.3$ for the R surface. The R surface that in reality consists of many larger pieces of rock against the background of a finer rocky material is more accurately characterized as a virtual object by a high value of a and a lower value of c . The M surface, with rocky pieces more uniform in size, is described in virtual terms by a high value of a c and the relatively low value of a . The cultivated surface (C), with furrows that were ploughed when the soil material was dry, contained many large soil aggregates and clods causing its high degree of roughness. Its virtual equivalent has a medium value, 0.5, of both a and c parameters. The parameter $b = 0.25$ does not illustrate the furrows real profile precisely enough. The shape of the furrows, with the depth of 10 cm and the distance between their successive tops of 60 cm, should be described by the $b = 0.2$, but accepting the b value 0.2 instead of 0.25 creates a higher rms error than 0.005 for all the analyzed wavelengths in the above procedure. The shape of the virtual surfaces expressed by parameters a , b , and c looks more realistic than that proposed in the previous geometrical models of Cierniewski, which utilized equal-sized spheroids of given horizontal and vertical radii, which were dispersed in a net of squares on a freely sloping plane, absorbed into the plane and having their tops at a height above it (Cierniewski & Karnieli, 2002; Cierniewski et al., 2002). In the Cierniewski et al. (2002) model that was designed to predict the directional reflectance from cultivated soils, the absorption along the direction of furrows is lower than that across it. The virtual surfaces created by these previous models from the measured directional reflectance data of uncultivated, as well as cultivated soils, appear as unrealistic, strongly vertical elongated spheroids.

The virtual surfaces of the tested types are characterized in terms of their surface shape directivity using the factor D_R , as well as the directivity of their hemispherical-directional reflectance distribution function D_{HDRDF} (Table 2). The cultivated surface with furrows is described by the highest values of both D_R and D_{HDRDF} . However, for the relatively smooth uncultivated surface (S), these functions have their lowest values. If the D_R increases for all the tested surfaces, ranging from the smoothest uncultivated (S) to the roughest cultivated with furrows (C), and is gradual and uniform, the growth of D_{HDRDF} is similarly uniform only for the uncultivated surfaces. Therefore, the difference in the directivity of HDRDF between of the uncultivated and cultivated surfaces is significant.

4. Summary and conclusion

The model presented in this paper predicts the normalized hemisphere-directional reflectance function for soil or rocky surfaces of a given roughness under outdoor illumination conditions. These surfaces are simulated by a virtual surface of geometrical shapes reminiscent of beads merging

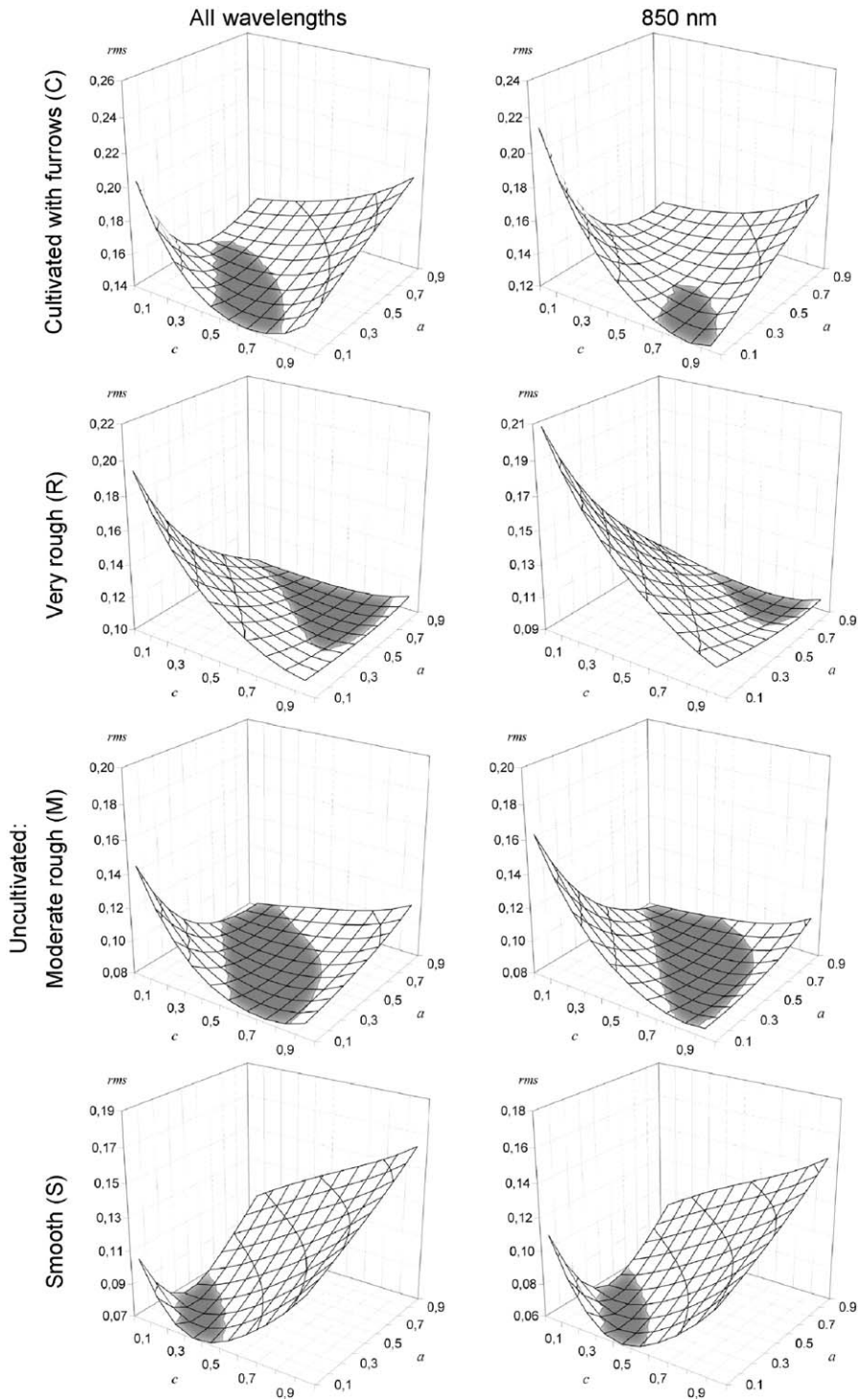


Fig. 14. Distribution of the root mean square error rms for measured and generated by the model reflectance data of the tested soil surfaces used in the fitting procedure of their virtual surface parameters. The shaded areas include the combinations of the parameters recovered with the error higher of 0.005 than the minimum rms.

into each other. The surfaces are constructed by sets of spheres of a given radius and position of their centers. The spheres are of equal size, and a given number are dispersed regularly in a net of squares. The height of the sphere centers is described by three geometrical parameters, a , b ,

and c . The a parameter describes the amplitude of the sinus function along the x -axis, and b describes that along the y -axis, relative to a . The c parameter describes the maximum deviation of the disturbance in the centers' height, in relation to values determined only by the parameters a

Table 2
Geometrical D_R and reflectance D_{HDRDF} directivity of the studied surfaces

Surfaces	D_R	D_{HDRDF}
Cultivated with furrows	0.10	0.27
Uncultivated very rough	0.07	0.19
Uncultivated moderate rough	0.04	0.17
Uncultivated relatively smooth	0.03	0.14

and b . The top of the simulated surface with elimination of any gaps between “beads merging into each other” is called the virtual surface. This surface is characterized by the mean deviation of its height along any direction. The differences between the maximum and the minimum values of the deviation calculated along all possible directions expresses the directivity of the surface shape D_R .

The surface is illuminated by a hemispherical light source, created by a number of point sources of given light intensities. The distribution of the hemispherical light is described by a formula that takes into account its amplification near the horizon, concentration inside the solar aureole near the sun, and the minimum in the quadrant opposite to the sun. The formula also takes into consideration the ratio of direct solar irradiance to global irradiance that varies with the sun’s position, as well as the normal optical thickness attributed to the wavelengths, and the quality and content of the aerosols in the atmosphere. Due to irregularities in the surface, it is impossible to completely illuminate it by all of the point sources on the hemisphere. A part of the light coming from these point sources might be blocked by the presence of adjoining fragments of the surface. The total amount of the light energy reaching the whole surface is the sum of the illumination effects of all of the elementary fragments of the surface, assuming that each of them can be illuminated by different unblocked light point sources. The light energy reaching the surface is scattered from it, according to the quasi-Lambertian function, i.e., a combination of the Lambertian scattering function and the quasi-specular scattering one.

The model assumes that the image of a whole surface, as viewed by a sensor suspended over it, is an effect of the reflectance of the incident energy in a given direction by a part of the elementary fragments of the surface lying inside the sensor’s field of view. The distribution of the surface reflectance, viewed from all the possible directions, is described by two view angles, the horizontal and the zenith, for all the possible illumination conditions. This distribution is expressed by the solar zenith angle and the horizontal angle for a given hemispherical light (described according to the parameters in the formula mentioned above), and is represented by the hemispherical–directional reflectance distribution function HDRDF of the surface. In this paper, these functions are normalized to the nadir viewing and visualized for a given illumination condition.

The model assumes that the HDRDF of a surface contains information about the directivity of the surface shape, which is quantitatively described by the directivity factor of the

surface hemispherical–directional reflectance function D_{HDRDF} . The D_{HDRDF} expresses the asymmetry of the HDRDF with respect to the SPP. The absolute differences in the surface reflectance Δ_{HDRDF} , viewed from two directions (described by the same value of the view zenith angle, but by different values of the view horizontal angle symmetrical to the SPP) are the elementary components of this asymmetry. The highest value of these maximum differences, calculated for a given hemispherical light distribution when the θ_S and the ϕ_S is changing gives this D_{HDRDF} factor. Both the directivity factors, the D_R and D_{HDRDF} , are strongly correlated, as shown by their high coefficient of determination r^2 is higher than 0.95. Probably, the model may reveal the directivities at a scale, which is difficult to observe by the human naked eye. However, the problem of the directivities at different roughness scales needs further studies.

The model was tested on directional reflectance data, measured in the visible, the near and the middle infrared ranges, for a cultivated surface with furrows and three uncultivated desert loess and rocky surfaces, situated in Israel. The model makes it possible to create from the measured data the synthetic surfaces, called virtual surfaces, described by the geometric parameters a , b , and c mentioned above. These virtual surfaces look quite similar to their real equivalents. As in reality, the virtual surface of the cultivated field has furrows, and the uncultivated ones do not have any. Furthermore, the higher the roughness of the real surfaces, the higher the roughness of their virtual equivalents. The cultivated surface with furrows has the highest values of the directivity factor of the surface shape D_R , as well as of the directivity factor of the hemispherical–directional reflectance function D_{HDRDF} . However, the relatively smooth uncultivated surface has these factors’ lowest values. The virtual equivalents of these surfaces, obtained from the spectral reflectance data, contain a degree of error, expressed by the root mean square rms, lower than 0.14 for the cultivated surface and not exceeding 0.10 for the uncultivated ones.

The hemispherical–directional reflectance model presented here, together with the virtual surfaces, being sets of the model input data describing the geometry of soil and rocky surfaces, enables us to predict realistic images of cultivated and uncultivated surfaces under given illumination and viewing conditions, as well as to distinguish the directivity in soil or rocky surface shapes from their directional reflectance data. However, this last potentiality of the model requires additional field reflectance and roughness tests on a larger number of surfaces with more diversified shapes, a careful evaluation of the measurement errors, as well as a possible verification of the model using other functions, describing the class of the surface shape.

The model could be used as a basis to create an operational tool for:

- completing soil reflectance data under illumination and viewing conditions that are difficult to collect and an accurate calculation of soil surface albedo; and

– converting soil remote sensing data recorded under different illumination and viewing conditions to standardized forms before classification procedure, that is particularly important for the data collected by air-borne and satellite sensors: wide field of view (FOV), narrow FOV tilted at different angles, and conical scanning.

Acknowledgements

This work was carried out within the framework of the projects: “Virtual surfaces for prediction of soil imageries in their variable illumination and viewing conditions” and “Sky irradiance distribution in the optical domain for modeling of the bidirectional reflectance from soil surfaces”, supported by Adam Mickiewicz, University in Poznań and the EC program “Improving Human Potential—Access to Research Infrastructure”. The authors wish to thank Dr. David Bonfil who enabled us to take measurements at the experimental farm, and also Mr. Aleksander Goldberg and Mr. Uri Gilead for their help in the field measurements.

References

- Abdou, W. A., Helmlinger, M. C., Conel, J. E., Bruegge, C. J., Pilorz, S. H., Martonchik, J. V., & Gaitley, B. J. (2000). Ground measurements of surface BRF and HDRF using PARABOLA III. *Journal of Geophysical Research*, *106*, 11967–11976.
- Abdou, W. A., Conel, J. E., Pilorz, S. H., Helmlinger, M. C., Brugge, C. J., Gaitley, B. J., Ledoboer, W. C., & Martonchik, J. V. (2001). Vicarious calibration. A reflectance-based experiment with AirMISR. *Remote Sensing of Environment*, *77*, 338–353.
- Brugge, C., Chrien, N., & Haner, D. (2001). A Spectralon BRF data base for MISR calibration applications. *Remote Sensing of Environment*, *76*, 354–366.
- Caulson, K. L. (1966). Effect of reflection properties of natural surfaces in aerial reconnaissance. *Applied Optics*, *5*, 905–917.
- Cierniewski, J. (1987). A model for soil surface roughness influence on the spectral response of bare soils in the visible and near-infrared range. *Remote Sensing of Environment*, *23*, 97–115.
- Cierniewski, J. (1989). An influence of the viewing geometry of bare rough soil surfaces on their spectral response in the visible and near-infrared range. *Remote Sensing of Environment*, *27*, 135–142.
- Cierniewski, J. (2001). *A directional reflectance model of cultivated soil surfaces taking into account their aggregates and micro-relief (in Polish)* (p. 150). Poznan: Bogucki Wydawnictwo Naukowe.
- Cierniewski, J., & Karnieli, A. (2002). Virtual surfaces simulating the bidirectional reflectance of semiarid soils. *International Journal of Remote Sensing*, *23/19*, 4019–4037.
- Cierniewski, J., Verbrugghe, M., & Marlewski, A. (2002). Effects of farming works on soil surface bidirectional reflectance measurements and modeling. *International Journal of Remote Sensing*, *23/6*, 1075–1094.
- Cooper, K. D., & Smith, J. A. (1985). A Monte Carlo reflectance model for soil surfaces with three-dimensional structure. *IEEE Transactions on Geoscience and Remote Sensing*, *1GE-23*, 668–676.
- Deering, D. W., Eck, T. F., & Otterman, J. (1990). Bidirectional reflectance of selected desert surfaces and their three-parameter soil characterization. *Agricultural and Forest Meteorology*, *52*, 71–90.
- Fraser, R. S. (1975). Interaction mechanisms—within the atmosphere (Chap. 5). *Manual of Remote Sensing* (pp. 181–233). Falls Church, VA: American Society of Photogrammetry.
- Grant, R. H., Gao, W., & Heisler, G. M. (1996). Photosynthetically-active radiation: Sky radiance distributions under clear and overcast conditions. *Agricultural and Forest Meteorology*, *82*, 267–292.
- Hapke, B., DiMucci, D., Nelson, R., & Smythe, W. (1996). The cause of the hot spot in vegetation canopies and soils: Shadow-hiding versus coherent backscatter. *Remote Sensing of Environment*, *58*, 63–68.
- Irons, J.R., & Smith, J.A. (1990). Soil surface roughness characterization from light scattering observations. *Proceedings of 10th Annual International Geosciences and Remote Sensing Symposium, May 20–24, 1990, Washington D.C., vol. II* (pp. 1007–1010).
- Irons, J. R., Campbell, G. S., Norman, J. M., Graham, D. W., & Kovalick, W. M. (1992). Prediction and measurement of soil bidirectional reflectance. *IEEE Transactions on Geoscience and Remote Sensing*, *30(2)*, 249–260.
- Kimes, D. S., & Sellers, P. J. (1985). Inferring hemispherical reflectance of the Earth’s surface for global energy budget from remotely sensed nadir or directional radiance values. *Remote Sensing of Environment*, *18*, 205–223.
- Kriebel, K. T. (1978). Measured spectral bidirectional reflection properties of four vegetated surfaces. *Applied Optics*, *17*, 253–259.
- Kriebel, K. T. (1996). On the limited validity of reciprocity in measured BRDFs. *Remote Sensing of Environment*, *58*, 52–62.
- Milton, E. J. (1989). Principles of field spectroscopy. *Remote Sensing Yearbook, 1988–1989* (pp. 79–99). London: Taylor & Francis.
- Milton, E. J., & Webb, J. P. (1987). Ground radiometry and airborne multispectral survey of bare soils. *International Journal of Remote Sensing*, *18*, pp. 3–14.
- Nicodemus, F. E. (1970). Reflectance nomenclature and directional reflectance and emissivity. *Applied Optics*, *9*, 1474–1475.
- Norman, J. M., Welles, J. M., & Walter, E. A. (1985). Contrast among bidirectional reflectance of leaves, canopies, and soils. *IEEE Transactions on Geoscience and Remote Sensing*, *GE-23*, 659–667.
- Otterman, J. (1981). Reflection from soil with sparse vegetation. *Advances in Space Resources*, *1*, 115–119.
- Sendmaier, S. R. (2000). Acquisition of bidirectional reflectance factor data with field goniometers. *Remote Sensing of Environment*, *73*, 257–269.
- Shoshany, M. (1991). The equifinality of bidirectional reflectance distribution functions of various microstructures. *International Journal of Remote Sensing*, *12*, 2267–2281.
- Shoshany, M. (1993). Roughness-reflectance relationship of bare desert terrain: An empirical study. *Remote Sensing of Environment*, *45*, 15–27.
- Strub, G., Beisl, U., Schaepman, M., Schlaepfer, D., Dickerhof, C., & Itten, K. (2002). Evaluation of diurnal hyperspectral HDRF data acquired with the RSL field goniometer during the DAISEX’99 campaign. *Photogrammetry and Remote Sensing*, *57*, 184–193.
- Strub, G., Schaepman, M. E., Knyazikhin, Y., & Itten, K. I. (2003). Evaluation of spectrodirectional alfalfa canopy data acquired during DAISEX’99. *IEEE Transactions on Geoscience and Remote Sensing*, *41*, 1034–1042.
- Zhang, Y., Tian, Y., Knyazikhin, Y., Marthonchik, J. V., Diner, D. J., Leroy, M., & Mynemi, R. B. (2000). Prototyping of MISR LAI and FPAR algorithm with POLDER data over Africa. *IEEE Transactions on Geoscience and Remote Sensing*, *38*, 2402–2418.